THE JOURNAL OF PHYSICAL CHEMISTRY B

Article

Cite This: J. Phys. Chem. B 2018, 122, 10044−10050

pubs.acs.org/JPCB

Volatility of Amorphous Solid Water

Mario Nachbar,*[,†,‡] Denis Duft,*[,‡] and Thomas Leisner[†,‡]

[†]Institute of Environmental Physics, University of Heidelberg, Im Neuenheimer Feld 229, 69120 Heidelberg, Germany

[‡]Institute of Meteorology and Climate Research, Karlsruhe Institute of Technology—KIT, P.O. Box 3640, 76021 Karlsruhe, Germany

Supporting Information

ABSTRACT: Amorphous solid water is probably the most abundant form of solid water in the universe. Its saturation vapor pressure and thermodynamic properties, however, are not well known. We have investigated the saturation vapor pressure over vapor-deposited amorphous ice at temperatures between 133 and 147 K using a novel experimental method. The new method determines the absolute vapor pressures and the sublimation rates by measuring the mass growth rates of ice-covered nanoparticles under supersaturated water vapor conditions. We find that the vapor pressure of amorphous solid water is up to a factor of 3 higher than that predicted by current parameterizations, which are based in part on calorimetric measurements. We demonstrate that the calorimetric measurements can be reconciled with our data by acknowledging the formation of nanocrystalline ice as an intermediate ice phase during the crystallization of amorphous ice. As a result, we propose a new value for the enthalpy of crystallization of amorphous solid water of $\Delta H = 2312 \pm 227$ J/mol, which is about 1000 J/mol higher than the current consensus. Our results shine a new light on the abundance of water ice clouds on Mars and mesospheric clouds on Earth and may alter our understanding of ice formation in the stratosphere.

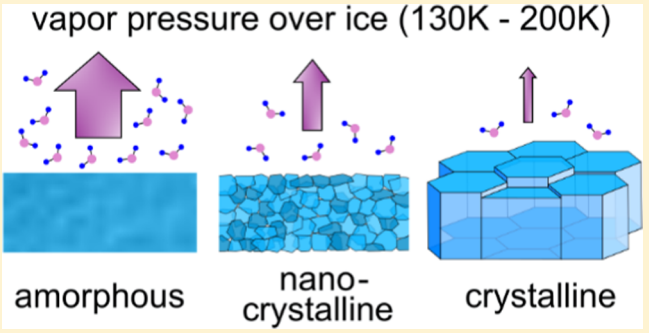

INTRODUCTION

Amorphous solid water (ASW) forms when water vapor condenses at low temperatures.[1] It is probably the most abundant form of solid water in the universe[1,2] and is thought to be a component of high altitude noctilucent clouds on Earth.[3] Due to the intriguing ubiquity of ASW, its saturation vapor pressure and the thermodynamics of the formation and sublimation processes have been the subject of numerous investigations. Most experimental studies have used indirect methods to determine the sublimation rates from ice surfaces rather than direct measurements of the vapor pressure under equilibrium conditions. These methods typically determine the change in mass or thickness during sublimation of water molecules from ice films using either quartz crystal microbalances,[4−7] quadrupole mass spectrometers,[5,8−13] or other techniques.[14] The frequently used parametrization by Murphy and Koop for the vapor pressure of ASW is in part based on the measurements of the latent heat release during the crystallization of ASW using differential scanning calorimetry (DSC).[15] However, despite all the efforts, reliable data for the absolute sublimation rate or the vapor pressure of ASW at temperatures below 150 K have remained elusive.

We recently introduced a new method for measuring the sublimation rate and thus the saturation vapor pressure of water deposits on solid surfaces at low temperatures.[16] The method relies on exposing small sub-4 nm nanoparticles at a well-defined temperature to water molecules evaporating from ice-covered sample surfaces. The change in nanoparticle mass is continuously monitored using a time-of-flight mass spectrometer. At high supersaturation, the nanoparticle ice growth rate is directly proportional to the water vapor partial pressure in the environment of the nanoparticles. Here, we present the measurements performed at low supersaturation, where the evaporation from the nanoparticles influences the nanoparticle ice growth rate. By fitting an ice growth model to the measured nanoparticle mass, we determine the saturation vapor pressure of the ice phase on the nanoparticles.

EXPERIMENTAL METHOD

In this work, we performed sublimation rate measurements of water ice that was deposited from the gas phase on small nanoparticles. We used the molecular flow ice cell-trapped reactive atmospheric particle spectrometer (MICE-TRAPS) apparatus, which was described earlier[17−20] and is only briefly recalled here. Sub-4 nm iron oxide (Fe_2O_3) and silica (SiO_2) particles are produced in a nonthermal low-pressure (60 mbar) helium microwave plasma from the metal−organic precursors ferrocene and tetraethylorthosilicate, respectively. It has been shown that metal-oxide nanoparticles produced in these types of sources under similar conditions are compact and spherical with a marginal degree of agglomeration.[21−23] The nano-

Received: July 5, 2018
Revised: October 4, 2018
Published: October 9, 2018

DOI: 10.1021/acs.jpcb.8b06387
J. Phys. Chem. B 2018, 122, 10044−10050

particles are transferred by means of an aerodynamic lens and a differential pumping stage into the trapped reactive atmospheric particle spectrometer (TRAPS). In TRAPS, particles carrying a single positive charge are mass selected with an electrostatic quadrupole deflector and stored in the molecular flow ice cell (MICE), which is a modified linear quadrupole ion trap. The particles stored in MICE exhibit a very narrow particle mass distribution with a standard deviation of less than 7%, which corresponds to 2.3% in the particle size distribution.[19] In MICE, the nanoparticles thermalize by collisions with a low-pressure He background gas. Additionally, the particles are exposed to a well-defined gas phase H_2O number density corresponding to supersaturated conditions. The H_2O number density is adjusted by temperature-controlled sublimation from surfaces that are coated with several microns of nanocrystalline water ice. The vapor pressure of this ice phase was characterized in a previous study,[16] ensuring an accuracy of n_{H_2O} of better than 10%. Once the nanoparticles are trapped in MICE, water molecules condense on the nanoparticle surface. The nanoparticle ice growth rate is measured by periodically extracting small portions of trapped nanoparticle population and measuring their mass with a time-of-flight mass spectrometer. The result is the particle mass as a function of the residence time in MICE. The mass range that can be investigated is limited by the voltages applied to MICE (frequency; amplitude; and extraction pulse timings). The settings are usually chosen to allow efficient trapping of particles with initial mass before water adsorption. In many cases, the ion signal obtained in a single measurement run is sufficient. Alternatively, multiple growth curves acquired with identical parameter settings can also be averaged offline. We did not observe a change in growth rates with time when analyzing the growth curves independently. This indicates that equilibrium of gas phase water concentration is obtained in MICE very quickly.

In our experiments, we use iron oxide and silica nanoparticles as core particles for the condensation of water ice. These materials exhibit a rather different density ($\rho_{Fe_2O_3}$ = 5.2 g/cm^3, ρ_{SiO_2} = 2.3 g/cm^3), which leads to different nanoparticle sizes when selecting the same initial particle mass. By comparing the results for both materials, we ensure that the choice of the particle material does not influence the outcome of the experiment.

■ ICE GROWTH MODEL

The rate of mass change of a particle in a H_2O background atmosphere is determined by the rates of deposition (k_{dep}) and sublimation (k_{sub}) of water molecules with mass m_{H2O} to and from the particle surface

$$\frac{dm}{dt} = [k_{dep} - k_{sub}]\cdot m_{H_2O} \tag{1}$$

In the molecular flow regime as employed in this experiment, the deposition rate k_{dep} is given by the product of particle surface area, water molecule flux density J_{in}, and the sticking probability α. The flux density can be expressed in terms of the number density n_{H_2O} and the mean thermal velocity of water molecules $v_{th} = \sqrt{8kT/\pi m_{H_2O}}$ leading to

$$k_{dep} = A_c\cdot J_{in}\cdot\alpha = A_c\cdot\frac{n_{H_2O}v_{th}}{4}\cdot\alpha \tag{2}$$

where $A_c = 4\pi(r + r_{coll})^2$ is the effective nanoparticle surface area of a spherical nanoparticle with radius r for collisions with water molecules. For the pick-up of water molecules by small nanoparticles in the size range of a few nanometer, the effective collision radius of water molecules r_{coll} = 1.5 Å[24] has to be taken into account. The sticking probability $\alpha = J_{ads}/J_{in}$ is defined as the probability that a water molecule colliding with a sample surface adsorbs and should not be confused with the condensation or uptake coefficient $\gamma = \alpha - J_{sub}/J_{in}$, with J_{sub} representing the sublimation flux density emitted by the ice sample (see Brown et al. (1996)[11] for a thorough discussion). For the temperatures investigated in this work (T < 160 K), values of α reported in the literature vary ($0.2 \le \alpha \le 1$).[11,25−32] However, in the overwhelming majority of these experiments (including one computer simulation that employs the TIP4P potential for water molecules), α is found to be close to unity ($\alpha = 0.99 \pm {}^{0.01}_{0.03}$).[11,25−28,31,32] It was also shown that under the conditions investigated in this work, the sticking probability is independent of the incident angle[25] and quickly approaches the bulk value, already at sub-monolayer coverages of thin water ice films on silica.[27] In the growth model, we therefore approximate the sticking probability to α = 1 and consider in the error estimation that it can be as low as α = 0.96.

The time-dependent nanoparticle radius r including the ice deposit can be calculated from the measured particle mass m assuming spherical ice particle growth and using the following relation

$$r^3(t) = \frac{3}{4\pi}\left(\frac{m_{ice}}{\rho_{ice}} + \frac{m_0}{\rho_0}\right) \tag{3}$$

where m_0 and ρ_0 are the initial mass and density of the nanoparticle before ice deposition and $m_{ice} = m - m_0$ is the mass of the condensed ice phase. The densities ρ_{ice} of the different ice polymorphs that may exist at the temperatures under investigation are known to be very similar[11,33] so that the nature of the deposited ice phase does not enter the calculation of the deposition rate.

To describe the sublimation rate, we assume that the particles are covered with an ice layer of sufficient thickness so that the properties of the outermost layer of water molecules are not influenced by the underlying substrate (see next section). Under this assumption, the sublimation rate in eq 1 is given by

$$k_{sub} = A\cdot\frac{p_{sat}v_{th}}{4kT}\cdot S_{eq} \tag{4}$$

where p_{sat} is the saturation vapor pressure over the nanoparticle ice phase at temperature T and $A = 4\pi r^2$ is the ice particle surface area. The equilibrium saturation S_{eq} takes into account the increased evaporation rate with respect to a flat surface due to the curvature of the nanoparticles by the Kelvin equation

$$S_{eq} = \exp\left(\frac{2\nu\sigma}{kTr}\right) \tag{5}$$

where ν is the molecular volume of the H_2O ice phase and σ is the surface tension of the interface between the water ice on the nanoparticles and the vapor phase. Recently, Factorovich and co-workers showed with a thermodynamic model that Kelvin effect calculations using the surface tension of bulk water are applicable down to about 0.5 nm in radius.[34] The curvature of the nanoparticles used in this study is considerable

DOI: 10.1021/acs.jpcb.8b06387
J. Phys. Chem. B 2018, 122, 10044−10050

and influences the desorption rate depending on the nanoparticle radius. The sublimation rate for ice particles (ASW, T = 140 K) comparable in size with the nanoparticles used in this work increases by a factor as large as S_{eq} = 4.8 for r = 2 nm and S_{eq} = 1.7 for r = 6 nm. The sensitivity of S_{eq} to the 2.3% uncertainty in particle radius is between 1 and 3%.

Combining eqs 1 through 5, we obtain the final expression for the growth model

$$\frac{dm}{dt} = \left[A_c \cdot \frac{n_{H_2O} v_{th}}{4} - A \cdot \frac{p_{sat} v_{th}}{4kT} \cdot \exp\left(\frac{2\nu\sigma}{kTr}\right)\right] \cdot m_{H_2O} \quad (6)$$

This is a nonlinear expression for the nanoparticle mass, as A and A_c are also functions of the particle mass m. Equation 6 can be integrated numerically to yield the particle mass as a function of time. In this work, we present measurements performed in conditions where the sublimation from the particle surface, represented by the second term on the right-hand side of eq 6, contributes substantially to the change in particle mass. We determine the saturation vapor pressure p_{sat} of the particle ice phase by fitting eq 6 to the growth rate data using the method of least squares.

Up to this point, we did not consider that the ice growth might be influenced by the charge residing on the nanoparticle. However, it is known that the equilibrium saturation of a dielectric liquid droplet is reduced for a charged droplet compared to a neutral droplet. The equation that describes the change in equilibrium saturation due to the droplet charge was first introduced by Thomson.[35] According to this now widely called classical Kelvin−Thomson equation in the Thomson liquid drop model (TLDM), the vapor pressure over a particle carrying a single central elementary charge is reduced by less than 0.5% compared to a neutral particle for the smallest particles investigated in this study. In recent years, modifications to the Kelvin−Thomson equation have been proposed to explain the experimental results obtained in cluster experiments and in experiments with small nanoparticles. However, by comparing the experimental data obtained from measurements of the binding enthalpy of water molecules on hydrated mono-, di-, and trivalent cluster ions, it was shown that the data were adequately represented by the Thomson liquid drop model.[36,37] As the estimated contribution due to the TLDM is very small for the particles in our study, we can neglect the charge effect in the derivation of the growth model.

DATA ANALYSIS

We measured the particle mass of iron oxide (Fe_2O_3) and silica (SiO_2) nanoparticles at supersaturated conditions in the temperature interval between 133 and 147 K. Figure 1 shows two typical growth curves measured for SiO_2 nanoparticles of different initial particle mass at different temperature and saturation S_h with respect to hexagonal ice. The monitored mass range is different for both growth curves as optimized parameter settings of MICE were chosen according to the different initial particle mass.

The particles are composed of SiO_2 and Fe_2O_3, which are hydrophilic materials with water adsorption enthalpies in the zero-coverage limit about 2 to 3 times higher than that of bulk H_2O.[27,38,39] Such materials are known to exhibit multilayer adsorption.[40] The differential desorption energies for SiO_2 and Fe_2O_3 decrease exponentially with water coverage and approach the value of bulk H_2O after about 0.5−1 monolayers,

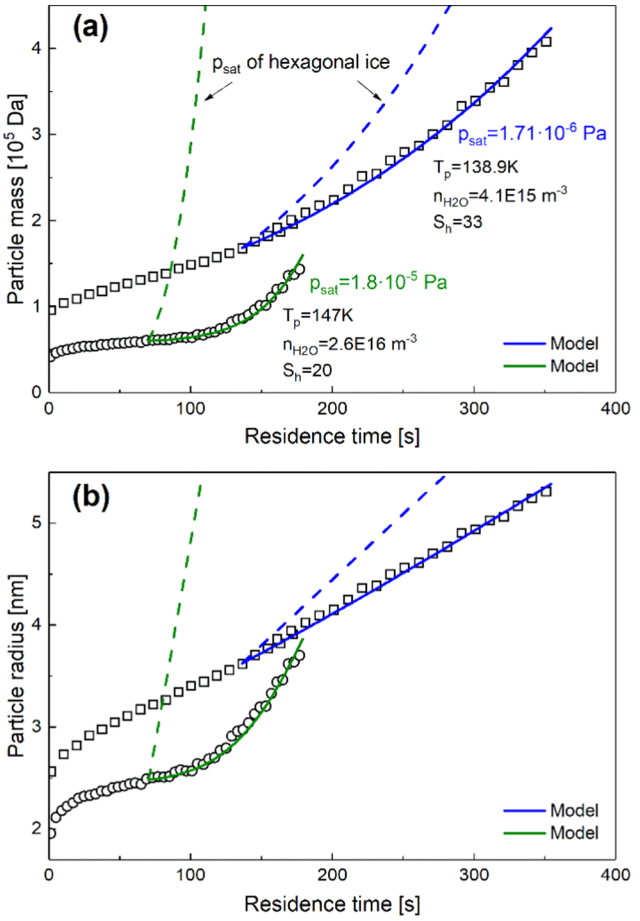

Figure 1. (a) Time evolution of nanoparticle mass under supersaturated conditions. For comparison, two growth curves at different initial particle mass, temperature, and saturation S_h with respect to hexagonal ice are shown. Dashed lines are results of the ice growth model (eq 6) using the surface tension and the vapor pressure of hexagonal ice. Solid lines are numerical fits of the growth model with the vapor pressure as the free parameter and using the parameterization for supercooled liquid water (SLW) (eq 8) for the surface tension of the ice−vapor interface. Panel (b) same as (a), but showing particle radius calculated from particle mass using eq 3.

thereby indicating the loss of information of the underlying substrate for higher coverages. We did not observe a significant alteration of the results when analyzing our data starting with a water ice coverage of two or three monolayers. We therefore analyzed all the data sets starting with a coverage between two and three monolayers and assume that the sublimation rate remains undisturbed by the underlying surface of the nanoparticle core.

According to the growth model (eq 6), two parameters govern the sublimation rate: the saturation vapor pressure and the surface tension of the ice phase on the particles. A priori, we do not know whether the ice phase on the nanoparticles is crystalline or amorphous. As a first attempt, we thus assumed the formation of crystalline ice. Consequently, we integrated eq 6 numerically to obtain the ice particle mass as a function of time using the surface tension of crystalline ice[41]

$$\sigma_{cryst} = (141 - 0.15 \cdot T\ [\mathrm{K}])\ (\mathrm{mN\ m^{-1}}) \quad (7)$$

and the well-established saturation vapor pressure of hexagonal ice.[15] The resulting calculated growth curves are shown as

DOI: 10.1021/acs.jpcb.8b06387
J. Phys. Chem. B 2018, 122, 10044−10050

dashed lines in Figure 1. The model results for hexagonal ice as the particle ice phase evidently disagree with the measured growth curves. The same result was obtained when considering cubic or stacking disordered ice.[42−46] We conclude that the particle ice phase is not represented by hexagonal ice, cubic, or stacking disordered ice. Because the observed particle growth rate is smaller than the model results, the sublimation rate needs to be higher than that for the crystalline ice phases. Therefore, we assume that amorphous ice forms on the nanoparticle surface.

Assuming the deposition of ASW provides the possibility to determine the sublimation rate of ASW by fitting the growth model to the experimental data. However, no measurements of the surface tension of ASW are available. Nevertheless, we can make use of the structural similarity between ASW and supercooled liquid water (SLW).[47,48] We assume that the surface tension of ASW is fairly well described by the surface tension of supercooled liquid water for which experimental data exist at warmer temperatures. Very recent measurements using two independent techniques showed that the surface tension of supercooled water follows a linear trend down to 250 K.[49−51] We fitted a linear trend to the surface tension data to extrapolate the temperature range in our experiments. The fitting procedure yields

$$\sigma_{SLW} = (114.81 - 0.144 \cdot T\ [\mathrm{K}])\ (\mathrm{mN\,m^{-1}}) \quad (8)$$

We allowed for an uncertainty of 10% for the surface tension of ASW and used eq 6 to numerically fit the saturation vapor pressure of ASW to the ice growth data. The resulting model growth curves are shown as solid lines in Figure 1. They are in excellent agreement with the measured data. We analyzed each growth curve as described above and normalized the fitted saturation vapor pressure to the well-known vapor pressure of hexagonal ice.[15] The resulting saturation vapor pressure typically has an uncertainty (1 standard deviation) of about 20%. The main error sources originate from the uncertainties of the gas phase H_2O concentration, the particle temperature ($\Delta p_{n,T} \sim 10\%$) and the surface tension ($\Delta p_{\sigma} \sim 10\%$). A list of the conditions applied in MICE and the corresponding experimental results is given in Table S1 in the Supporting Information (SI).

RESULTS AND DISCUSSION

In total, 15 experiments were performed for $S_h < 60$ using SiO_2 and Fe_2O_3 nanoparticles with initial particle radii between 1.8 and 2.6 nm in the temperature interval between 133 and 147 K. The fitted normalized saturation vapor pressures of the ice phase deposited on the particles are shown as full red circles in Figure 2.

We find that the saturation vapor pressure of the ice phase deposited on the particles is 5 to 10 times higher than the saturation vapor pressure of hexagonal ice. The saturation vapor pressure p_{sat}^{m} of a metastable ice phase is related to a difference in the enthalpy $\Delta H_{m\to h}$ and a difference in the entropy $\Delta S_{m\to h}$ to the stable hexagonal ice (p_{sat}^{hex}) according to

$$\frac{p_{sat}^{m}}{p_{sat}^{hex}} = \exp\left(\frac{\Delta G_{m\to h}}{RT}\right) = \exp\left(\frac{\Delta H_{m\to h} - T\cdot\Delta S_{m\to h}}{RT}\right) \quad (9)$$

By fitting our data, we find $\Delta H_{m\to h} = 2960 \pm 660$ J/mol and $\Delta S_{m\to h} = 5.0 \pm 4.7$ J/mol/K (not included in Figure 2).

Figure 2 also reproduces our previous results on the saturation vapor pressure over ice-covered surfaces[16] (blue

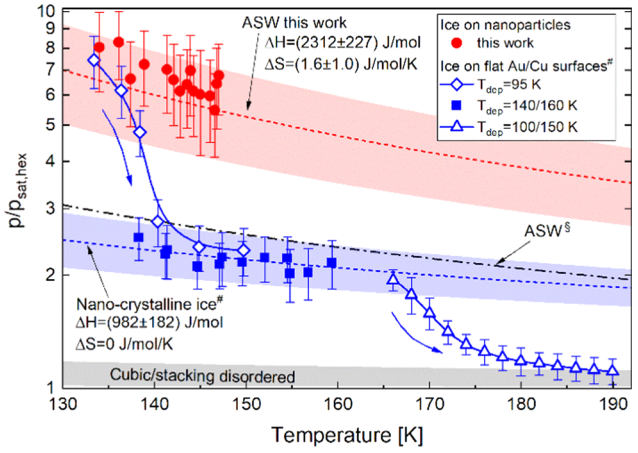

Figure 2. Saturation vapor pressure of vapor-deposited ASW and ice crystallized from ASW. #Ice deposited on Au/Cu surfaces from Nachbar et al.[16] Arrows indicate the chronology of measurements. Solid lines are splines added as a guide to the eye. T_{dep} indicates the deposition temperature of the ice sample. The red and blue shaded areas represent the 1σ uncertainty interval. §Parameterization based on DSC measurements.[15]

symbols). Here, no assumption on the surface tension of the ice sample was made. After initial deposition of ASW at 95 K, we observe a decrease in vapor pressure between 134 and 140 K (open blue diamonds). We attributed this transition to the crystallization of ASW. Crystallization is a temperature-activated two-step process of nucleation and subsequent growth of crystal embryos within the amorphous solid. The vapor pressure of the resulting metastable ice phase is about 2.5 times higher than the vapor pressure of hexagonal ice. The same ice phase may be produced if water vapor is deposited at warmer temperatures (full blue squares). According to eq 9, this ice phase is characterized by an enthalpy difference $\Delta H_{n\to h} = 982 \pm 182$ J/mol and an insignificant entropy difference with respect to hexagonal ice (dashed blue line). We showed previously that this ice phase is consistent with nanocrystalline ice with crystal diameters between 7 and 19 nm. The increased vapor pressure of nanocrystalline ice is a consequence of the high-surface-energy-to-volume-energy ratio of the nanocrystals. At temperatures below 160 K, the crystal size and thus the vapor pressure remains stable for many hours.[16,52] Only at temperatures above 165 K, the nanocrystals grow on time scales accessible in the laboratory leading to macroscopic ice crystals with a vapor pressure consistent with expectations for cubic/stacking disordered ice[15,53−57] (open blue triangles).

At 133 K, the saturation vapor pressure of the nanoparticle ice phase agrees well with the saturation vapor pressure of ASW on the flat ice sample before crystallization (Figure 2, leftmost open blue diamond symbol), leading us to conclude that the water deposited on the nanoparticles is indeed ASW. In contrast to the previous experiments on macroscopic deposits, the ASW did not crystallize on the nanoparticles up to a deposition temperature of 147 K, the maximum temperature accessible in this type of experiment. In the ice nanoparticle experiments presented in this work, the measurement time was much shorter than the typical crystallization time. This explains the prevalence of ASW on the ice particles in these experiments. A comparison of measurement time and typical crystallization times is given in the Supporting Information (SI).

DOI: 10.1021/acs.jpcb.8b06387
J. Phys. Chem. B 2018, 122, 10044−10050

Our findings show that the vapor pressure of ASW is a factor of 2 to 3 times higher than previous estimates represented by the parameterization of Murphy and Koop[15] (black dash-dotted line in Figure 2). For the temperature range of interest, the parameterization of Murphy and Koop is based on differential scanning calorimetry (DSC) measurements of the heat release during the crystallization of ASW. Such measurements report an enthalpy of crystallization of around ΔH = 1330 J/mol.[53,58−61] In the following, we show how these DSC data can be reconciled with our findings if the intermediate phase of nanocrystalline ice is taken into account.

Differential scanning calorimetry measures the heat capacity of the ice sample as a function of temperature during warm-up. Phase transitions are identified as either positive or negative peaks in DSC signals, according to endothermic (melting) or exothermic transitions (crystallization). The temperature at which crystallization occurs as well as the peak width depends on the heating rate. The enthalpy of crystallization can be obtained by integrating the heat capacity difference of the ice sample before and after crystallization. In Figure 3a, we

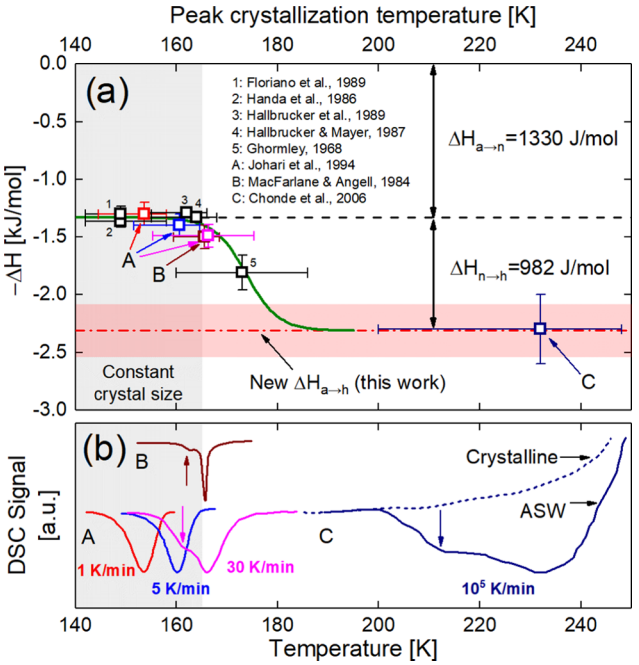

Figure 3. Literature survey of DSC measurements using ASW samples. Panel (a) shows the enthalpy released during crystallization of ASW.[53,58−64] Note that one result of Johari et al. (1994) and the data point of MacFarlane and Angell (1984) overlap. The green solid line was added as a guide to the eye. Panel (b) shows representative DSC raw signals. The data were scaled and shifted vertically for visibility reasons. Vertical arrows indicate the appearance of a second peak.

reproduce literature results on the crystallization enthalpy ΔH obtained with the DSC measurements employing ASW samples. The data are shown as a function of the peak crystallization temperature, with the temperature error bar reflecting the peak width of the DSC measurements. Figure 3b shows the representative DSC traces for various heating rates. Standard DSC setups apply a heating rate between 0.5 and 30 K/min. At these heating rates, the crystallization of ASW peaks between about 150 and 170 K. It is known that nanocrystalline ice forms when the crystallization of ASW occurs at these temperatures.[16] This fact, however, has not been considered in the DSC studies. After complete (nano-)crystallization below 165 K, crystal growth is suppressed on laboratory time scales. Above 165 K, crystal growth in the nanocrystalline ice polymorph requires tens of minutes to hours.[16,52] For typical DSC heating rates, the DSC measurements are conducted within minutes and thus the heat release associated with crystal growth subsequent to the initial nanocrystallization may be overlooked in conventional DSC measurements. Consequently, the DSC measurements, with crystallization occurring below 165 K (gray shaded area in Figure 3a,b), only detect the enthalpy difference between ASW and nanocrystalline ice. The DSC measurements with peak crystallization temperatures above 165 K[61−64] show a second peak in the DSC traces (marked by vertical arrows in Figure 3b), with an associated increase in ΔH. This may indicate that crystallization at temperatures above 165 K directly leads to larger crystal sizes. Ultrafast DSC measurements allow for heating rates up to 10^5 K/s, where crystallization of ASW to macrocrystalline ice occurs between 200 and 250 K (curve C in Figure 3b). Here, a crystallization enthalpy for ASW of $\Delta H_{a\rightarrow h}$ = 2300 ± 300 J/mol was reported.[62] This value is in good agreement with the enthalpy difference between ASW and hexagonal ice of $\Delta H_{a\rightarrow h}$ = 2960 ± 660 J/mol found from the vapor pressure measurements reported in this study.

In conclusion, we argue that the enthalpy difference ΔH = 1330 ± 45 J/mol (black dashed line in Figure 3a) determined in classical DSC experiments with peak crystallization temperatures below 165 K reflects the transition from amorphous to nanocrystalline ice. Adding to this the enthalpy difference for the transition from nanocrystalline ice to hexagonal ice of $\Delta H_{n\rightarrow h}$ = 982 ± 182 J/mol from our previous work yields a total enthalpy difference for the transition from amorphous to hexagonal ice of $\Delta H_{a\rightarrow h}$ = 2312 ± 227 J/mol (red dash-dotted line in Figure 3a). This value agrees well with the ultrafast DSC results from Chonde et al.[62] ($\Delta H_{a\rightarrow h}$ = 2300 ± 300 J/mol). As a result, we propose a new parameterization for the vapor pressure of ASW using eq 9 with $\Delta H_{a\rightarrow h}$ = 2312 ± 227 J/mol and $\Delta S_{a\rightarrow h}$ = 1.6 ± 1.0 J/mol/K.[12] Here, the well-established parameterization for the vapor pressure of hexagonal ice serves as a reference. The crystallization enthalpy is based on the DSC measurements and our previously reported parameterization for nanocrystalline ice, as it provides a smaller uncertainty interval compared to the direct measurements presented in this study. This parameterization for the saturation vapor pressure of ASW is shown in Figure 2 as a dashed red line. No significant difference in the heat capacity of ASW and crystalline ice has been reported between 60 and 200 K.[56,62] Therefore, $\Delta H_{a\rightarrow h}$ and $\Delta S_{a\rightarrow h}$ are constant between 60 and 200 K and the proposed parameterization should be valid in this temperature range.

CONCLUSIONS

We conclude that ASW has a higher vapor pressure than previously assumed. Furthermore, the results support our earlier conclusion that for T < 160 K, water vapor initially deposits as ASW. Consequently, the formation of ice particles at these temperatures is dominated by the properties of ASW rather than crystalline ice. This finding has important implications for the modeling of cloud formation in planetary atmospheres. For example, water ice clouds frequently form at temperatures below 160 K in the terrestrial mesopause[65,66] and on Mars.[67−69] Additionally, the saturation vapor pressure of

DOI: 10.1021/acs.jpcb.8b06387
J. Phys. Chem. B 2018, 122, 10044−10050

ASW is important to describe the sublimation of interstellar ice.[2,13,70] Our findings also have implications for the understanding of the vapor pressure of supercooled liquid water at warmer temperatures. If adapted accordingly, the calculated values for the vapor pressure of supercooled water will increase substantially even at temperatures as warm as 200 K, with a potentially significant impact on modeling of stratospheric cloud formation.

■ ASSOCIATED CONTENT

Supporting Information

The Supporting Information is available free of charge on the ACS Publications website at DOI: 10.1021/acs.jpcb.8b06387.

Comparison of ASW crystallization rate and measurement time (Text S1); measurement data (Table S1) (Figure 2) (PDF)

■ AUTHOR INFORMATION

Corresponding Authors

*E-mail: mario.nachbar@kit.edu (M.N.).
*E-mail: denis.duft@kit.edu (D.D.).

ORCID

Denis Duft: 0000-0003-2943-3574

Notes

The authors declare no competing financial interest.

■ ACKNOWLEDGMENTS

The authors thank the German Federal Ministry of Education and Research (BMBF, grant numbers 05K13VH3 and 05K16VHB) and the German Research Foundation (DFG, grant number LE 834/4-1) for financial support of this work.

■ REFERENCES

(1) Angell, C. A. Amorphous Water. *Annu. Rev. Phys. Chem.* **2004**, *55*, 559−583.
(2) Burke, D. J.; Brown, W. A. Ice in Space: Surface Science Investigations of the Thermal Desorption of Model Interstellar Ices on Dust Grain Analogue Surfaces. *Phys. Chem. Chem. Phys.* **2010**, *12*, 5947−5969.
(3) Murray, B. J.; Jensen, E. J. Homogeneous Nucleation of Amorphous Solid Water Particles in the Upper Mesosphere. *J. Atmos. Sol.-Terr. Phys.* **2010**, *72*, 51−61.
(4) Bryson, C. E.; Cazcarra, V.; Levenson, L. L. Sublimation Rates and Vapor Pressures of Water, Carbon Dioxide, Nitrous Oxide, and Xenon. *J. Chem. Eng. Data* **1974**, *19*, 107−110.
(5) Sack, N. J.; Baragiola, R. A. Sublimation of Vapor-Deposited Water Ice Below 170 K, and Its Dependence on Growth Conditions. *Phys. Rev. B* **1993**, *48*, 9973−9978.
(6) Perry, R.; Meadows, G.; Mosier, L.; Woronowicz, M. In *Measurement of Cryogenic Ice Sublimation Using Quartz Crystal Microbalances*, SPIE Optical Engineering + Applications; SPIE, 2012; 849208.
(7) Woronowicz, M.; Meadows, G. In *Application of Astm E-1559 Apparatus to Study H2O Desorption*, SPIE Optical Engineering + Applications; SPIE, 2012; 849209.
(8) Löfgren, P.; Ahlström, P.; Lausma, J.; Kasemo, B.; Chakarov, D. Crystallization Kinetics of Thin Amorphous Water Films on Surfaces. *Langmuir* **2003**, *19*, 265−274.
(9) Kouchi, A. Vapour Pressure of Amorphous H2O Ice and Its Astrophysical Implications. *Nature* **1987**, *330*, 550−552.
(10) Speedy, R. J.; Debenedetti, P. G.; Smith, R. S.; Huang, C.; Kay, B. D. The Evaporation Rate, Free Energy, and Entropy of Amorphous Water at 150 K. *J. Chem. Phys.* **1996**, *105*, 240−244.
(11) Brown, D. E.; George, S. M.; Huang, C.; Wong, E. K. L.; Rider, K. B.; Smith, R. S.; Kay, B. D. H2O Condensation Coefficient and Refractive Index for Vapor-Deposited Ice from Molecular Beam and Optical Interference Measurements. *J. Phys. Chem.* **1996**, *100*, 4988−4995.
(12) Smith, R. S.; Matthiesen, J.; Knox, J.; Kay, B. D. Crystallization Kinetics and Excess Free Energy of H2O and D2O Nanoscale Films of Amorphous Solid Water. *J. Phys. Chem. A* **2011**, *115*, 5908−5917.
(13) Fraser, H. J.; Collings, M. P.; McCoustra, M. R. S.; Williams, D. A. Thermal Desorption of Water Ice in the Interstellar Medium. *Mon. Not. R. Astron. Soc.* **2001**, *327*, 1165−1172.
(14) White, B. E., Jr.; Hessinger, J.; Pohl, R. O. Annealing and Sublimation of Noble Gas and Water Ice Films. *J. Low Temp. Phys.* **1998**, *111*, 233−246.
(15) Murphy, D. M.; Koop, T. Review of the Vapour Pressures of Ice and Supercooled Water for Atmospheric Applications. *Q. J. R. Meteorol. Soc.* **2005**, *131*, 1539−1565.
(16) Nachbar, M.; Duft, D.; Leisner, T. The Vapour Pressure over Nano-Crystalline Ice. *Atmos. Chem. Phys.* **2018**, *18*, 3419−3431.
(17) Duft, D.; Nachbar, M.; Eritt, M.; Leisner, T. A Linear Trap for Studying the Interaction of Nanoparticles with Supersaturated Vapors. *Aerosol Sci. Technol.* **2015**, *49*, 683−691.
(18) Meinen, J.; Khasminskaya, S.; Ruehl, E.; Baumann, W.; Leisner, T. The Traps Apparatus: Enhancing Target Density of Nanoparticle Beams in Vacuum for X-Ray and Optical Spectroscopy. *Aerosol Sci. Technol.* **2010**, *44*, 316−328.
(19) Nachbar, M.; Duft, D.; Mangan, T. P.; Martin, J. C. G.; Plane, J. M. C.; Leisner, T. Laboratory Measurements of Heterogeneous CO2 Ice Nucleation on Nanoparticles under Conditions Relevant to the Martian Mesosphere. *J. Geophys. Res.: Planets* **2016**, *121*, 753−769.
(20) Nachbar, M.; Duft, D.; Kiselev, A.; Leisner, T. Composition, Mixing State and Water Affinity of Meteoric Smoke Analogue Nanoparticles Produced in a Non-Thermal Microwave Plasma Source. *Z. Phys. Chem.* **2018**, *232*, 635−648.
(21) Giesen, B.; Wiggers, H.; Kowalik, A.; Roth, P. Formation of Si-Nanoparticles in a Microwave Reactor: Comparison between Experiments and Modelling. *J. Nanopart. Res.* **2005**, *7*, 29−41.
(22) Janzen, C.; Kleinwechter, H.; Knipping, J.; Wiggers, H.; Roth, P. Size Analysis in Low-Pressure Nanoparticle Reactors: Comparison of Particle Mass Spectrometry with in Situ Probing Transmission Electron Microscopy. *J. Aerosol Sci.* **2002**, *33*, 833−841.
(23) Nadeem, K.; Krenn, H.; Traussnig, T.; Wurschum, R.; Szabo, D. V.; Letofsky-Papst, I. Spin-Glass Freezing of Maghemite Nanoparticles Prepared by Microwave Plasma Synthesis. *J. Appl. Phys.* **2012**, *111*, No. 113911.
(24) Bickes, R. W.; Duquette, G.; van den Meijdenberg, C. J. N.; Rulis, A. M.; Scoles, G.; Smith, K. M. Molecular Beam Scattering Experiments with Polar Molecules: Measurement of Differential Collision Cross Sections for H2O+H2, He, Ne, Ar, H2O and NH3 +H2, He, NH3. *J. Phys. B: At. Mol. Phys.* **1975**, *8*, 3034−3043.
(25) Batista, E. R.; Ayotte, P.; Bilić, A.; Kay, B. D.; Jónsson, H. What Determines the Sticking Probability of Water Molecules on Ice? *Phys. Rev. Lett.* **2005**, *95*, No. 223201.
(26) Gibson, K. D.; Killelea, D. R.; Yuan, H.; Becker, J. S.; Sibener, S. J. Determination of the Sticking Coefficient and Scattering Dynamics of Water on Ice Using Molecular Beam Techniques. *J. Chem. Phys.* **2011**, *134*, No. 034703.
(27) Sneh, O.; Cameron, M. A.; George, S. M. Adsorption and Desorption Kinetics of H2O on a Fully Hydroxylated SiO2 Surface. *Surf. Sci.* **1996**, *364*, 61−78.
(28) Hundt, P. M.; Bisson, R.; Beck, R. D. The Sticking Probability of D2O-Water on Ice: Isotope Effects and the Influence of Vibrational Excitation. *J. Chem. Phys.* **2012**, *137*, No. 074701.
(29) Chaix, L.; van den Bergh, H.; Rossi, M. J. Real-Time Kinetic Measurements of the Condensation and Evaporation of D2O Molecules on Ice at 140 K < T < 220 K. *J. Phys. Chem. A* **1998**, *102*, 10300−10309.

DOI: 10.1021/acs.jpcb.8b06387
J. Phys. Chem. B 2018, 122, 10044−10050

(30) Pratte, P.; van den Bergh, H.; Rossi, M. J. The Kinetics of H2O Vapor Condensation and Evaporation on Different Types of Ice in the Range 130−210 K. *J. Phys. Chem. A* **2006**, *110*, 3042−3058.
(31) Tolbert, M. A.; Middlebrook, A. M. Fourier Transform Infrared Studies of Model Polar Stratospheric Cloud Surfaces: Growth and Evaporation of Ice and Nitric Acid/Ice. *J. Geophys. Res.: Atmos.* **1990**, *95*, 22423−22431.
(32) Bryson, C. E.; Cazcarra, V.; Levenson, L. L. Condensation Coefficient Measurements of H2O, N2o, and CO2. *J. Vac. Sci. Technol.* **1974**, *11*, 411−416.
(33) Loerting, T.; Bauer, M.; Kohl, I.; Watschinger, K.; Winkel, K.; Mayer, E. Cryoflotation: Densities of Amorphous and Crystalline Ices. *J. Phys. Chem. B* **2011**, *115*, 14167−14175.
(34) Factorovich, M. H.; Molinero, V.; Scherlis, D. A. Vapor Pressure of Water Nanodroplets. *J. Am. Chem. Soc.* **2014**, *136*, 4508−4514.
(35) Thomson, J. J.; Thomson, G. P. *Conduction of Electricity through Gases*; Cambridge University Press: London, 1906.
(36) Donald, W. A.; Williams, E. R. Evaluation of Different Implementations of the Thomson Liquid Drop Model: Comparison to Monovalent and Divalent Cluster Ion Experimental Data. *J. Phys. Chem. A* **2008**, *112*, 3515−3522.
(37) Heiles, S.; Cooper, R. J.; DiTucci, M. J.; Williams, E. R. Sequential Water Molecule Binding Enthalpies for Aqueous Nanodrops Containing a Mono-, Di- or Trivalent Ion and between 20 and 500 Water Molecules. *Chem. Sci.* **2017**, *8*, 2973−2982.
(38) Mazeina, L.; Navrotsky, A. Enthalpy of Water Adsorption and Surface Enthalpy of Goethite (α-FeOOH) and Hematite (α-Fe2O3). *Chem. Mater.* **2007**, *19*, 825−833.
(39) Navrotsky, A.; Mazeina, L.; Majzlan, J. Size-Driven Structural and Thermodynamic Complexity in Iron Oxides. *Science* **2008**, *319*, 1635−1638.
(40) Venables, J. A.; Spiller, G. D. T.; Hanbucken, M. Nucleation and Growth of Thin Films. *Rep. Prog. Phys.* **1984**, *47*, 399−459.
(41) Hale, B. N.; Plummer, P. L. M. Molecular Model for Ice Clusters in a Supersaturated Vapor. *J. Chem. Phys.* **1974**, *61*, 4012−4019.
(42) Hudait, A.; Qiu, S. W.; Lupi, L.; Molinero, V. Free Energy Contributions and Structural Characterization of Stacking Disordered Ices. *Phys. Chem. Chem. Phys.* **2016**, *18*, 9544−9553.
(43) Kuhs, W. F.; Sippel, C.; Falenty, A.; Hansen, T. C. Extent and Relevance of Stacking Disorder in "Ice I-C". *Proc. Natl. Acad. Sci. U.S.A.* **2012**, *109*, 21259−21264.
(44) Lupi, L.; Hudait, A.; Peters, B.; Grünwald, M.; Gotchy Mullen, R.; Nguyen, A. H.; Molinero, V. Role of Stacking Disorder in Ice Nucleation. *Nature* **2017**, *551*, 218−222.
(45) Malkin, T. L.; Murray, B. J.; Salzmann, C. G.; Molinero, V.; Pickering, S. J.; Whale, T. F. Stacking Disorder in Ice I. *Phys. Chem. Chem. Phys.* **2015**, *17*, 60−76.
(46) Thürmer, K.; Nie, S. Formation of Hexagonal and Cubic Ice During Low-Temperature Growth. *Proc. Natl. Acad. Sci. U.S.A.* **2013**, *110*, 11757−11762.
(47) Urquidi, J.; Benmore, C. J.; Egelstaff, P. A.; Guthrie, M.; McLain, S. E.; Tulk, C. A.; Klug, D. D.; Turner, J. F. C. A Structural Comparison of Supercooled Water and Intermediate Density Amorphous Ices. *Mol. Phys.* **2004**, *102*, 2007−2014.
(48) Soper, A. K. Supercooled Water: Continuous Trends. *Nat. Mater.* **2014**, *13*, 671−673.
(49) Hrubý, J.; Vinš, V.; Mareš, R.; Hykl, J.; Kalová, J. Surface Tension of Supercooled Water: No Inflection Point Down to −25 °C. *J. Phys. Chem. Lett.* **2014**, *5*, 425−428.
(50) Vinš, V.; Fransen, M.; Hykl, J.; Hrubý, J. Surface Tension of Supercooled Water Determined by Using a Counterpressure Capillary Rise Method. *J. Phys. Chem. B* **2015**, *119*, 5567−5575.
(51) Vinš, V.; Hošek, J.; Hykl, J.; Hrubý, J. Surface Tension of Supercooled Water: Inflection Point-Free Course Down to 250 K Confirmed Using a Horizontal Capillary Tube. *J. Chem. Eng. Data* **2017**, *62*, 3823−3832.
(52) Hansen, T. C.; Koza, M. M.; Lindner, P.; Kuhs, W. F. Formation and Annealing of Cubic Ice: II. Kinetic Study. *J. Phys.: Condens. Matter* **2008**, *20*, No. 285105.
(53) Handa, Y. P.; Klug, D. D.; Whalley, E. Difference in Energy between Cubic and Hexagonal Ice. *J. Chem. Phys.* **1986**, *84*, 7009−7010.
(54) Shilling, J. E.; Tolbert, M. A.; Toon, O. B.; Jensen, E. J.; Murray, B. J.; Bertram, A. K. Measurements of the Vapor Pressure of Cubic Ice and Their Implications for Atmospheric Ice Clouds. *Geophys. Res. Lett.* **2006**, *33*, No. L17801.
(55) McMillan, J. A.; Los, S. C. Vitreous Ice - Irreversible Transformations During Warm-Up. *Nature* **1965**, *206*, 806−807.
(56) Sugisaki, M.; Suga, H.; Seki, S. Calorimetric Study of Glassy State.4. Heat Capacities of Glassy Water and Cubic Ice. *Bull. Chem. Soc. Jpn.* **1968**, *41*, 2591−2599.
(57) Mayer, E.; Hallbrucker, A. Cubic Ice from Liquid Water. *Nature* **1987**, *325*, 601−602.
(58) Floriano, M. A.; Handa, Y. P.; Klug, D. D.; Whalley, E. Nature of the Transformations of Ice-I and Low-Density Amorphous Ice to High-Density Amorphous Ice. *J. Chem. Phys.* **1989**, *91*, 7187−7192.
(59) Hallbrucker, A.; Mayer, E. Calorimetric Study of the Vitrified Liquid Water to Cubic Ice Phase-Transition. *J. Phys. Chem.* **1987**, *91*, 503−505.
(60) Hallbrucker, A.; Mayer, E.; Johari, G. P. Glass-Liquid Transition and the Enthalpy of Devitrification of Annealed Vapor-Deposited Amorphous Solid Water - a Comparison with Hyperquenched Glassy Water. *J. Phys. Chem.* **1989**, *93*, 4986−4990.
(61) Johari, G. P.; Fleissner, G.; Hallbrucker, A.; Mayer, E. Thermodynamic Continuity between Glassy and Normal Water. *J. Phys. Chem.* **1994**, *98*, 4719−4725.
(62) Chonde, M.; Brindza, M.; Sadtchenko, V. Glass Transition in Pure and Doped Amorphous Solid Water: An Ultrafast Microcalorimetry Study. *J. Chem. Phys.* **2006**, *125*, No. 094501.
(63) Ghormley, J. A. Enthalpy Changes and Heat-Capacity Changes in Transformations from High-Surface-Area Amorphous Ice to Stable Hexagonal Ice. *J. Chem. Phys.* **1968**, *48*, 503−508.
(64) Macfarlane, D. R.; Angell, C. A. Nonexistent Glass-Transition for Amorphous Solid Water. *J. Phys. Chem.* **1984**, *88*, 759−762.
(65) Rapp, M.; Lübken, F. J. Polar Mesosphere Summer Echoes (PMSE): Review of Observations and Current Understanding. *Atmos. Chem. Phys.* **2004**, *4*, 2601−2633.
(66) Lübken, F.-J.; Lautenbach, J.; Höffner, J.; Rapp, M.; Zecha, M. First Continuous Temperature Measurements within Polar Mesosphere Summer Echoes. *J. Atmos. Sol.-Terr. Phys.* **2009**, *71*, 453−463.
(67) Maltagliati, L.; Montmessin, F.; Fedorova, A.; Korablev, O.; Forget, F.; Bertaux, J. L. Evidence of Water Vapor in Excess of Saturation in the Atmosphere of Mars. *Science* **2011**, *333*, 1868−1871.
(68) Vincendon, M.; Pilorget, C.; Gondet, B.; Murchie, S.; Bibring, J. P. New near-Ir Observations of Mesospheric CO2 and H2O Clouds on Mars. *J. Geophys. Res.: Planets* **2011**, *116*, No. E00J02.
(69) Guzewich, S. D.; Talaat, E. R.; Toigo, A. D.; Waugh, D. W.; McConnochie, T. H. High-Altitude Dust Layers on Mars: Observations with the Thermal Emission Spectrometer. *J. Geophys. Res.: Planets* **2013**, *118*, 1177−1194.
(70) Léger, A.; Gauthier, S.; Defourneau, D.; Rouan, D. Properties of Amorphous H2O Ice and Origin of the 3.1 μm Absorption. *Astron. Astrophys.* **1983**, *117*, 164−169.

DOI: 10.1021/acs.jpcb.8b06387
J. Phys. Chem. B 2018, 122, 10044−10050